Ammonia monitoring near 1.5 μm with diode-laser absorption sensors

Michael E. Webber, Douglas S. Baer, and Ronald K. Hanson

We investigated ammonia spectroscopy near 1.5 μm to select transitions appropriate for trace ammonia detection in air-quality and combustion emissions-monitoring applications using diode lasers. Six ammonia features were selected for these trace-gas detection applications based on their transition strengths and isolation from interfering species. The strengths, positions, and lower-state energies for the lines in each of these features were measured and compared with values published in the literature. Ammonia slip was measured in the exhaust above an atmospheric pressure premixed ethylene–air burner to demonstrate the feasibility of the *in situ* diode-laser sensor. © 2001 Optical Society of America

OCIS codes: 300.6260, 300.6390.

1. Introduction

Ammonia is an important species for the refrigeration and fertilizer industries, as well as for NO_x removal in postcombustion gases. Ammonia's widespread use and toxic nature introduce a need to monitor its presence so that pollution and human health risks can be minimized. Ammonia sensors benefit industrial air quality by detecting leaks and unhealthy ambient ammonia concentrations before health damage occurs. Selective noncatalytic reduction systems, also known as Thermal DeNO$_x$,[1] inject ammonia at a specific temperature window downstream of combustion to destroy NO_x populations. Sensors are needed to monitor the emission of excess unconverted ammonia—ammonia slip—that pollutes the environment. Because of their capacity for subsecond, accurate, sensitive, species-specific, and *in situ* measurements, diode-laser sensors based on absorption spectroscopy offer advantages for monitoring potentially harmful ammonia concentrations in both the industrial and the Thermal DeNO$_x$ environments.

When this research was performed, all the authors were with the High Temperature Gasdynamics Laboratory, Department of Mechanical Engineering, Stanford University, Stanford, California 94305-3032. M. E. Webber (webber@pranalytica.com) is now with Pranalytica, Inc., 1101 Colorado Avenue, Santa Monica, California 90401-3009. D. S. Baer is now with Informed Diagnostics, 1050 East Duane Avenue, Suite I, Sunnyvale, California 94086.

Received 10 July 2000; revised manuscript received 2 December 2000.

0003-6935/01/122031-12$15.00/0

In situ measurement techniques are attractive for NH_3 because of difficulties involved with the measurement of NH_3 from hot flue gases by use of extractive sampling probes. Some of these difficulties are discussed by Hjuler and Dam-Johansen[2] and Kassman *et al.*[3] and include adsorption of NH_3 along the sampling lines, which hinders the sensor's ability to track transients; formation of salts that clog the sampling lines because of reactions between NH_3 and other flue gas constituents; decomposition of NH_3 in the sampling probes; and gas transport time, which slows down the sensor's overall response time. Sensors that can measure *in situ* avoid the above-mentioned challenges, but are susceptible to beam steering caused by gradients in the flow and possible spectral interference from the hot combustion products CO_2 and H_2O.

In this research we seek to aid in the design of near-infrared NH_3 sensors by carefully analyzing the absorption band near 1.5 μm to select isolated NH_3 transitions for use with diode-laser absorption sensors. Once the appropriate transitions were identified, we measured their fundamental spectroscopic parameters, such as line strength, line position, and lower-state energy. Sample measurements of NH_3 slip were then made in postcombustion exhaust gases to demonstrate the feasibility of the sensors and the isolation of the selected NH_3 transitions.

2. Theory

The fundamental theory governing absorption spectroscopy is embodied in the Beer–Lambert law, Eq. (1), and is described thoroughly by Nagali *et al.*[4]

Table 1. Coefficients of the Polynomial Expression for $Q(T)$ in Eq. (5)

	Hitran96[a]		Gamache[b]	
Coefficient	$70 < T < 500$ K	$500 < T < 1500$ K	$70 < T < 500$ K	$500 < T < 1500$ K
a	-42.037	-471.39	-62.293	-0.59594×10^{-4}
b	2.5976	5.4035	3.0915	32.387
c	0.013073	6.4491×10^{-3}	9.4575×10^{-3}	-4.0459×10^{-2}
d	-6.2223×10^{-6}	-7.2674×10^{-7}	1.8416×10^{-6}	3.1843×10^{-5}

[a]Ref. 10.
[b]Ref. 5.

The ratio of the transmitted intensity I_t and initial (reference) intensity I_0 of laser radiation through an absorbing medium at a particular frequency is related exponentially to the transition line strength S_i ($\mathrm{cm}^{-2}\ \mathrm{atm}^{-1}$), line-shape function ϕ (cm), total pressure P (atm), mole fraction of the absorbing species x_j, and path length L (cm):

$$\frac{I_t}{I_0} = \exp(-S_i \phi P x_j L). \tag{1}$$

The two laser intensities can be converted to absorbance $\alpha(\nu)$ and related to the transition parameters by

$$\alpha(\nu) = -\ln(I_t/I_0) = S_i \phi P x_j L. \tag{2}$$

The NH_3 line strength as a function of temperature for the ith transition is governed by its line strength at a reference temperature $S_i(T_0)$, ammonia's partition function $Q(T)$, the frequency of the transition $\nu_{0,i}$, and the lower-state energy of the transition E_i''. This relationship is given by

$$S_i(T) = S_i(T_0)\,\frac{Q(T_0)}{Q(T)}\left(\frac{T_0}{T}\right)\exp\left[-\frac{hcE_i''}{k}\left(\frac{1}{T}-\frac{1}{T_0}\right)\right] \times \left[1-\exp\left(\frac{-hc\nu_{0,i}}{kT}\right)\right]\left[1-\exp\left(\frac{-hc\nu_{0,i}}{kT_0}\right)\right]^{-1}. \tag{3}$$

The total internal partition function $Q(T)$ can be described by classical means as a product of the nuclear, rotational, and vibrational partition functions Q_{nuc}, Q_{rot}, and Q_{vib}, respectively [Eq. (4)], or approximated by a third-order polynomial [Eq. (5)], for which the coefficients a, b, c, and d are listed in Table 1:

$$Q(T) = Q_{\mathrm{nuc}} Q_{\mathrm{rot}} Q_{\mathrm{vib}}, \tag{4}$$

$$Q(T) = a + bT + cT^2 + dT^3. \tag{5}$$

Figure 1 plots the classical partition function [Eq. (4)] and the approximated partition function [Eq. (5)] over a range of temperatures from 300 to 1000 K. The partition function based on polynomial coefficients from Hitran96 in Table 1 underestimates the classically approximated partition function by ~10% at 500 K and ~40% at 1000 K because it does not include the contributions of the vibrational partition function.[5,6] By use of updated coefficients provided by Gamache[5], and also listed in Table 1, the polynomial expression and the classical model differ by less than 2% throughout the temperature range. Superimposed on the plot is an estimate for the total partition function at 300, 500, and 1000 K that uses McDowell's detailed rotational partition function sums, but includes contributions from nitrogen spin (McDowell's published sums include spin contributions only from the H atoms) and the vibrational partition function.[7] The values based on McDowell's calculations agree well with both the classical model and with the polynomial expression by use of Gamache's coefficients. Thus we conclude that Gamache's partition function is more accurate than the data in Hitran96.

3. Experimental Setup

Figure 2 shows the basic experimental schematic that was used for all the static cell measurements. The diode-laser system consisted of an external-cavity diode laser (ECDL) with a spectral tuning range of 1496–1582 nm (6321–6684 cm^{-1}). We could tune the ECDL over its entire optical range by adjusting its internal grating with a piezoelectrically controlled motor. For individual line-shape measurements (approximately 1-cm^{-1} scans), a sawtooth voltage waveform modulated the internal grating with a piezoactuator (injection current, 55 mA; case temperature, 23 °C).

The ECDL output passed through an optical isolator (−30-dB isolation) to prevent backreflections from

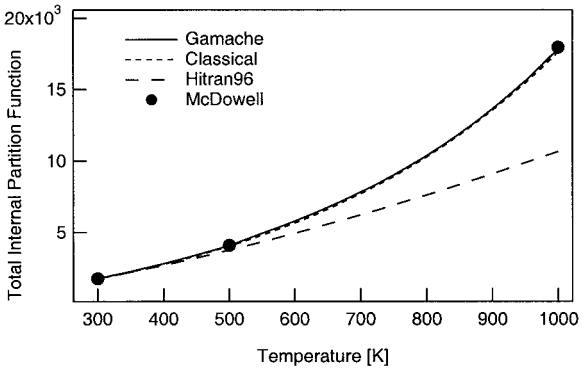

Fig. 1. Comparison of the partition function values from Hitran96,[10] the classical model (rigid rotor and simple harmonic oscillator), McDowell,[7] and Gamache.[5]

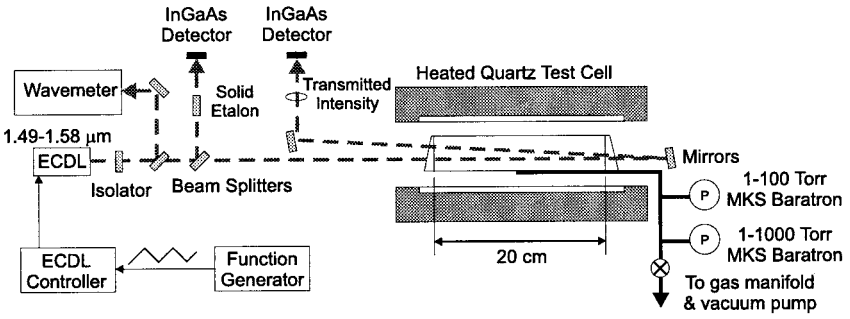

Fig. 2. Experimental schematic for measuring absorption spectra of NH_3 at a range of pressures and temperatures.

returning to the laser cavity. Beam splitters split the isolated ECDL output and directed one path to the IR wavelength meter for measuring the laser frequency and directed another path through the solid etalon (a free spectral range of 2.01 GHz) for monitoring the wavelength variations during laser tuning. Approximately 80% of the radiation was transmitted through the static cell to monitor NH_3 absorption. InGaAs detectors (300-kHz bandwidth) were used to measure the laser intensity at the end of the etalon and transmission paths, low-pass analog filters prevented signal aliasing, and a 12-bit digital oscilloscope was used for data acquisition.

Room-temperature measurements were made with the heater off and with several different cells and configurations, including a 20-cm quartz cell with double-pass alignment, a 15-cm stainless-steel cell in triple- and quintuple-pass alignment, and a single-pass 50-cm quartz cell. We avoided unwanted interference fringes that are due to etaloning in the transmission path by mounting 0.5° wedged windows at a 3° (or greater) angle on the cells. Two MKS Baratron pressure gauges with operational ranges of 100 and 1000 Torr, respectively, and accuracies of $\pm 1\%$ monitored the test cell pressure at all times.

Ammonia's adsorption on the chamber walls decreased the pressure after samples were introduced into the test cell. By monitoring the system pressure at all times and using pure gas samples (specified at 99.99% purity by Matheson) instead of calibrated mixtures for the static cell measurements, we avoided ammonia concentration uncertainty that is attributable to this adsorption. Several minutes after we filled the cell with NH_3, the pressure varied slowly enough to permit absorption measurements with an accurate estimate of the ammonia number density in the optical path.

For the survey spectra measurements (see Fig. 4), we used a 50-cm quartz cell in a single-pass configuration, and we scanned the ECDL across its entire optical range. For high-temperature static cell measurements, the 20-cm quartz cell in double-pass alignment was used exclusively to avoid the catalyzed dissociation of NH_3 that would occur with heated metal cells.[8] Four type S thermocouples, equally spaced along the cell axis, were used to monitor the cell temperature at all times. We determined the temperature deviations along the 20-cm cell to be $<2\%$ by traversing a thermocouple along the cell. Gases were allowed to heat for at least 30 min to achieve a steady and uniform gas temperature inside the cell.

4. Line Selection

The different environments in which ammonia monitoring is pertinent—air-quality monitoring for industrial applications and emissions monitoring for Thermal DeNO_x applications—have different conditions and challenges. For air-quality monitoring, the environment is typically a factory floor, a fertilizer facility, or an outdoor stockyard. The conditions for these environments are atmospheric pressure and room temperature (0–40 °C) and have potential spectroscopic interferences from atmospheric water.

For emissions monitoring, the environment is typically in a postcombustion exhaust stack, with a pressure slightly above 1 atm and a temperature range between 300 and 1250 K. The interfering species for this application are the major products of combustion, namely, CO_2 and H_2O.

We need to select NH_3 transitions that avoid approximately 1–2% of atmospheric water for the first application and 10–20% each of hot H_2O and CO_2 for the latter. Lines suitable for application in an ammonia sensor must avoid these interfering species and have suitable line strengths for sensitive trace-gas detection. For both applications, understanding the temperature sensitivities and line strengths is required for accurate sensors.

Ammonia's spectroscopy in the near IR is complicated, with many strong and overlapping lines that are difficult to resolve. Moreover, spectroscopic databases such as GEISA[9] and Hitran96[10] do not contain ammonia's near-IR spectra. Although there are many published papers that discuss NH_3 monitoring at 1.5 μm,[11–21] and many papers that address fundamental NH_3 spectroscopy at other wavelengths,[22–37] few investigate the fundamental spectroscopic parameters at 1.5 μm. However, two papers by Lundsberg-Nielsen *et al.* are available that catalog extensively the lines, positions, and strengths of NH_3 absorption at 1.5 μm.[38,39] Unfortunately, this research was performed in the optically thick regime, distorting the line-strength measurements for the strongest NH_3 lines and making the features difficult to resolve. Moreover, a recent paper by Modugno

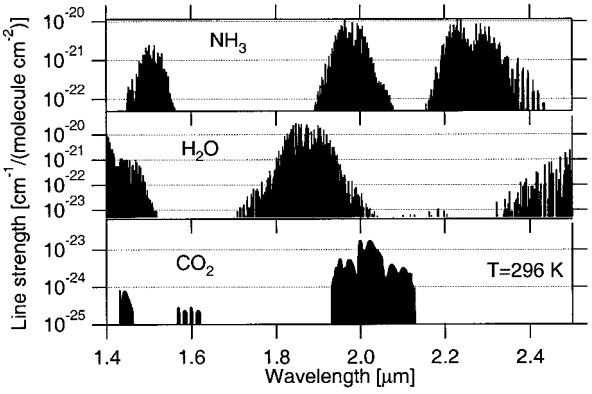

Fig. 3. Ammonia, water, and carbon dioxide line strengths in the near IR.[10,38,39]

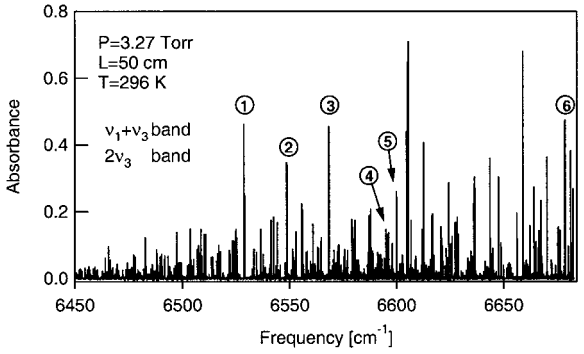

Fig. 4. Survey spectra of pure ammonia near 1.5 μm (P = 3.27 Torr, L = 50 cm, T = 296 K). The six features that were selected for atmospheric and emissions monitoring are marked on the plot and listed in Table 2.

and Corsi[21] investigated two regions of the 1.5-μm band (6475–6494 and 6685–6700 cm^{-1}) but did not include a study of the many strong NH_3 lines between these ranges.

Figure 3 depicts the new-IR line strengths of ammonia, water, and carbon dioxide from 1.4 to 2.5 μm in wavelength. Three main bands of ammonia are present in this region at 1.5, 2.0, and 2.3 μm, respectively. The line strengths for Fig. 3 are from Lundsberg-Nielsen *et al*. for the 1.5-μm band of NH_3[38,39] and from Hitran96 for the 2.0- and 2.3-μm bands of ammonia and all the H_2O and CO_2 bands.[10] A weak ammonia combination band is also present at 1.65 μm (Ref. 40); however, a detailed listing of line positions and strengths for this region is not currently available.

Of the three regions, 2.3 and 1.5 μm are the most useful for emissions monitoring of ammonia slip because of the relative scarcity and weakness of the interfering species' transitions. In contrast, at 2.0 μm H_2O and CO_2 interferences are substantial, eliminating this region as a viable option for emissions monitoring. All three bands, however, are suitable for air-quality monitoring. All three bands, however, are suitable for air-quality monitoring. The interfering presence of H_2O at 1.4 μm tapers off near 1.5 μm; and the CO_2 line strengths in this region are fairly weak, allowing for isolated NH_3 transitions in postcombustion gases. At 2.3 μm there is almost no CO_2 absorption; and the water lines are weaker and less populated, leaving spectral windows available for interference-free NH_3 absorption. Although the NH_3 line strengths at 2.3 μm are a few times larger than at 1.5 μm, the commercial availability and field-tested durability of room-temperature diode lasers at the shorter wavelengths[41] make the 1.5-μm region a superior choice at present for commercial sensor development and application.

Figure 4 shows a survey spectrum of ammonia transitions over the 1492–1550-nm (6450–6700-cm^{-1}) range that was recorded with the ECDL. Most of these transitions are a part of the $\nu_1 + \nu_3$ and $2\nu_3$ combination and overtone bands, although other bands such as the $2\nu_1$, $\nu_1 + 2\nu_4$, and $\nu_3 + 2\nu_4$ are also present.[23,39] By overlaying the measured survey spectra with calculated H_2O and CO_2 absorbance for the two applications, we can identify different ammonia features that are useful for interference-free monitoring. Six NH_3 features are indicated on this survey: three that are appropriate for emissions-monitoring applications and three for air-quality monitoring. Table 2 lists the feature locations and the applications for which they are useful.

The top panel of Fig. 5 shows three isolated and pressure-broadened NH_3 features that are useful for emissions monitoring overlaid with the calculated spectral interference of H_2O and CO_2. Of the combustion products, H_2O typically offers the most spectral interference in the near IR. Thus stoichiometric methane–air combustion product populations (19% H_2O, 9.5% CO_2) were used to model the interference spectra. The calculated interference was based on Hitran96 line strengths at a temperature of T = 400 K (Ref. 10) and stoichiometric methane–air combustion product populations for H_2O and CO_2. The bottom panel of Fig. 5 shows three NH_3 features overlaid with the calculated interference for 85% standard humidity conditions (X_{H_2O} = 2.2%).

All six features are isolated from interfering species and have line strengths that are suitable for sensitive detection over 1-m path lengths at temperatures below 600 K ($S_i > 0.01$ cm^{-2} atm^{-1}). Their high-resolution spectra and multiline Voigt peak fits are shown in Fig. 6. Of the three suitable air-quality

Table 2. Locations of Six NH_3 Features and Their Appropriate Monitoring Applications

Feature	Location (cm^{-1})	Location (nm)	Application
1	6528.9	1531.7	Air-quality monitoring
2	6548.7	1527.0	Emissions monitoring
3	6568.4	1522.4	Air-quality monitoring
4	6596.4	1516.0	Emissions monitoring
5	6600.0	1515.2	Emissions monitoring
6	6678.4	1497.4	Air-quality monitoring

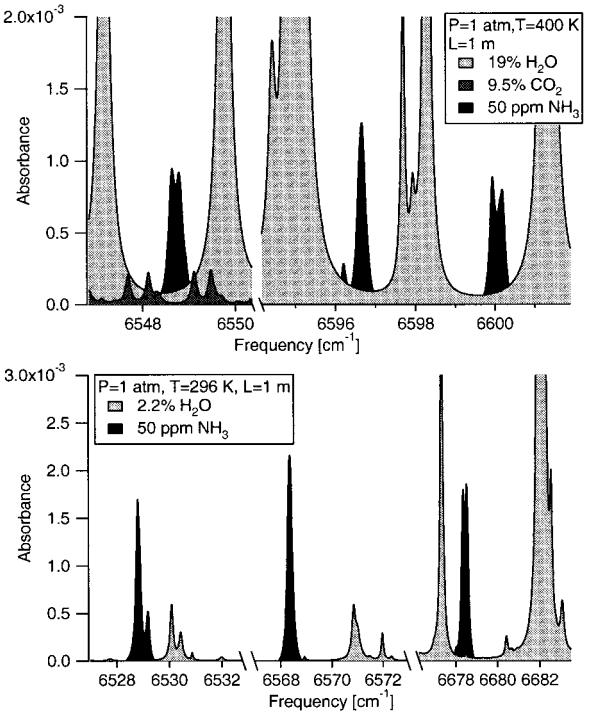

Fig. 5. Top panel: measured ammonia features at 6548, 6596, and 6600 cm^{-1} overlaid with the calculated absorbances of X_{H_2O} = 19% and X_{CO_2} = 9.5% for the products of a stoichiometric methane–air flame. Bottom panel: measured ammonia features at 6528, 6568, and 6678 cm^{-1} overlaid with the absorbance of X_{H_2O} = 2.2% corresponding to 85% standard atmospheric humidity. ppm, parts per million.

monitoring features, the one at 6528 cm^{-1} offers the best balance between overall feature strength and limited blending, thereby simplifying the peak-fitting process. The lines at 6548 cm^{-1} are the best choice for emissions monitoring because they have the least interference from combustion species, have less blending than the other two features, and are relatively strong, even at elevated temperatures. The latter lines are approximately twice as strong as the best lines identified by Modugno and Corsi.[21]

5. Spectroscopic Results

Before an ammonia sensor could be developed, the positions, strengths, and lower-state energies of the absorption lines contained in each of the six above-mentioned NH_3 features needed to be verified. The first task was to use high-resolution spectroscopy at room temperature and low pressures to determine the number of lines contained in each NH_3 feature, as well as their individual line strengths and positions.

As Figs. 4 and 6 demonstrate, the near-IR spectrum of NH_3 is crowded and contains many overlapping transitions. The multitude of lines is a result of ammonia's inversion doubling[42] and the coincidence of several harmonic and combination bands at 1.5 μm, including the $\nu_1 + \nu_3$, $2\nu_3$, and $\nu_3 + 2\nu_4$ bands.[23,38] Moreover, ammonia's strong dipole creates broad line shapes as a result of dipole–dipole interactions during collisions,[25,28,29,43,44] causing many of these neighboring lines to overlap.

The six features shown in Fig. 6 are typical exam-

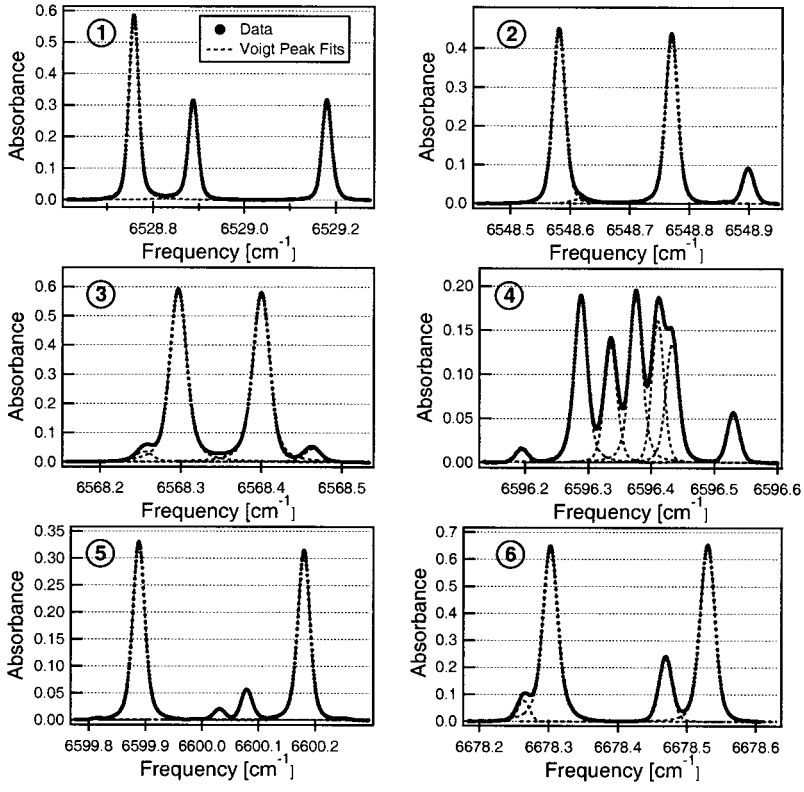

Fig. 6. Recorded high-resolution spectra and multiline Voigt fits of the six ammonia features selected for monitoring in atmospheric and combustion applications (pure NH_3, P = 5.6 Torr, L = 40 cm, T = 20 °C).

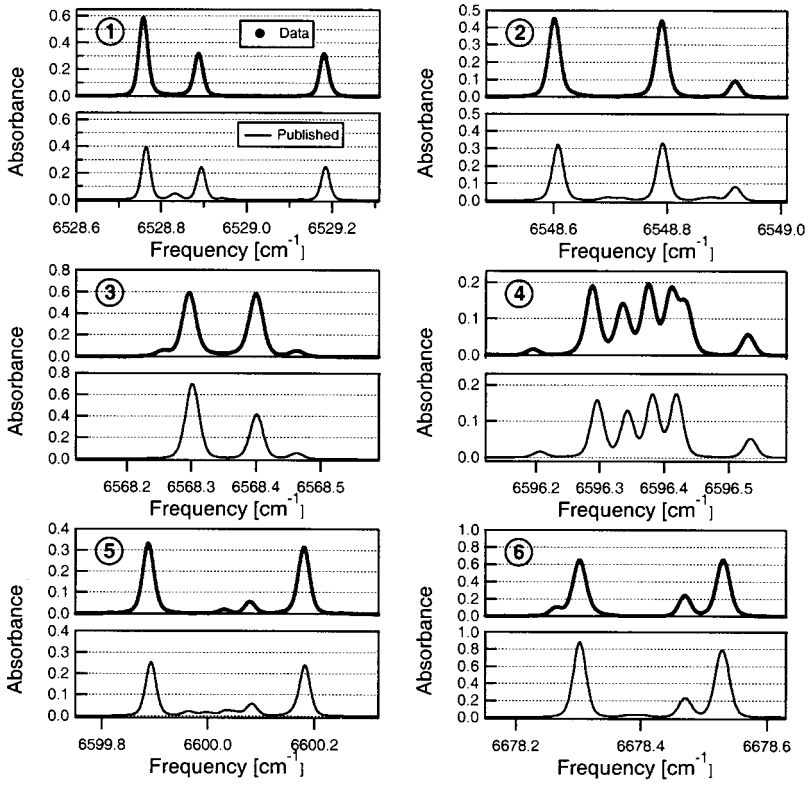

Fig. 7. Comparison of measured spectra for the six features in Table 2 with the calculated spectra based on line strengths and positions from Refs. 38 and 39 and broadening coefficients from Refs. 28, 29, 43, and 44 (pure NH_3, $P = 5.6$ Torr, $L = 40$ cm, $T = 20$ °C).

ples of the spectra near 1.5 μm. All six features have several lines close together in frequency, many of which cannot be isolated completely even at low pressures. At the higher pressures that will be prevalent for the monitoring applications, these lines become strongly blended. Determination of the spectroscopic parameters of each individual transition within these overlapping features thus requires high-resolution spectroscopy that employs low pressures (1–15 Torr) and longer path lengths. Typical single-sweep data for these high-resolution scans are shown in Fig. 6. Because of the blended nature of the features, multiline Voigt peak fits were needed to extract the integrated area for each individual transition, and thus the line strength S_i. These individual fits are illustrated as broken curves for each feature in Fig. 6.

The uncertainty for many of the individual line-strength measurements was estimated to be <3% because of measurement uncertainties of 1% in the total pressure, 1% in the total path length, and 1% in the area under each Voigt profile. The measurement uncertainty based on spread in the data agreed with the expected uncertainty for strong and isolated lines at room temperature. However, for strong lines that are blended, such as those in the feature at 1516 nm, the difficulties in the accurate determination of the baseline and separation of the areas of different transitions increase the uncertainty to 5–6% at room temperature. For lines that are both weak and blended, we estimate the uncertainty to be 10–12%. At higher temperatures, hot lines emerge, crowding the six spectral features and further increasing the line-strength measurement uncertainties.

Figure 7 compares the measured spectra for the six features in Table 2 with calculated spectra based on the published line positions and strengths in Lundsberg-Nielsen et al.[38,39] and the average published broadening parameters of $\gamma_{NH_3-NH_3} = 0.45$ and $\gamma_{NH_3-N_2} = 0.10$ cm^{-1} atm^{-1}.[28,29,43,44] In general, the published and measured features agree qualitatively in shape and position. However, there are many differences that emerge with regard to the number of lines in each feature and in the specific line positions and line strengths of the individual lines. The recorded spectra of the six features, as determined by this research, contain 26 transitions (see Tables 3–8), five of which were not listed by Lundsberg-Nielsen *et al*. Moreover, Lundsberg-Nielsen *et al*. list an additional 14 transitions that were not observed during our research.

The biggest differences between the published values and the results in this research occur wherever there are blended features. For isolated transitions of moderate strength ($0.005 < S < 0.06$), such as the lines at 6548.92, 6568.46, and 6596.53 cm^{-1}, the measured line positions and strengths agree with the published values. Features that blend a strong line with a weak line, such as 6548.6, 6568.3, and 6678.3 cm^{-1}, are listed by Lundsberg-Nielsen *et al*. as two equally strong lines. The resolved spectra in this

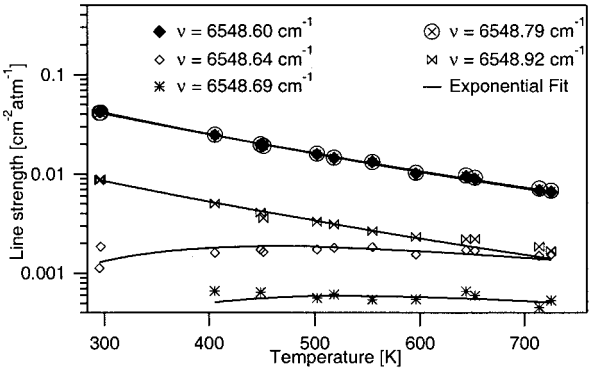

Fig. 8. Line strength versus temperature for the five lines in the NH_3 feature at 6548 cm^{-1} (1527 nm).

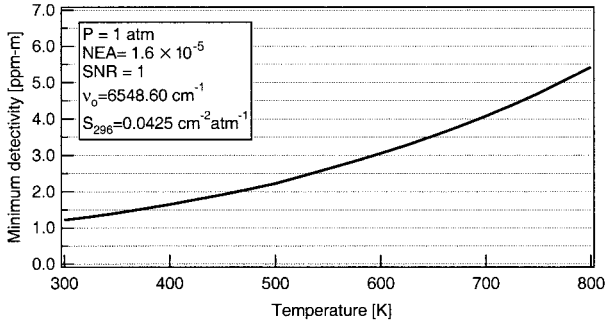

Fig. 9. Minimum detectivity versus temperature over a 1-m path for the line at $\nu = 6548.60\ cm^{-1}$ by use of the measured lower-state energy $E'' = 210\ cm^{-1}$ and a NEA of 1.6×10^{-5}.

research elucidate the blending and relative line strengths of these neighboring lines. For the feature at 6596.4 cm^{-1}, the previously published research fails to include the two distinct lines at 6596.41 and 6596.43 cm^{-1}, instead listing them as one combined line at 6596.42 cm^{-1}. Moreover, Lundsberg-Nielsen *et al*. list weak lines near 6528.83, 6548.70, 6599.96 and 6678.38 cm^{-1} that were not seen in the recorded spectra in our research. In addition, the line strengths of the individual strong lines listed in Lundsberg-Nielsen *et al*. are often underpredicted by as much as 10–20% compared with the line strengths measured in our research. Because the room-temperature measurements presented here were made in the optically thin regime and with low experimental uncertainty, we consider them to represent improvements over previously published values.

Because ammonia monitoring is pertinent for a range of elevated temperatures, the determination of how the NH_3 line strengths change as a function of temperature is important. For each feature, the line strengths were measured at 5–11 temperatures between room temperature and 725 K, with three to five different pressures at each temperature. The strongest lines in each of the six NH_3 features decreased in strength with increasing temperature; however, most features had weak lines that became stronger and some had hot lines that were not measurable at room temperature, but then became visible at the elevated temperatures.

Figure 8 shows the variations in line strength with increasing temperature for the lines in the feature near 6548 cm^{-1} (1527 nm). The three strongest room-temperature lines (6548.60, 6548.79, and 6548.92 cm^{-1}) decrease in strength with increasing temperature, whereas the weakest line (6548.64 cm^{-1}) gains strength, and a fifth hot line (6548.69 cm^{-1}) that was not measured at the lower temperatures emerges at higher temperatures.

Using the data for the measured line strengths as a function of temperature and Eqs. (3) and (5), we performed an exponential fit for each transition to determine the best-fit room-temperature reference line strength S_0 and the lower-state energy E''. Of the 35 lines in the six features, Lundsberg-Nielsen *et al*. assigned nine of them to the $\nu_1 + \nu_3$ band. Using these assignments and the lower-state energies calculated by Urban *et al*.,[32] yields the assigned lower-state energies.

The measured lower-state energies in this research were compared with the assigned lower-state energies as a check on the accuracy of the line assignment, and they agreed within uncertainty for four of the lines, but disagreed for five of the lines. For the disagreements, the measured values were 20–40% higher than the assigned values. The disagreements were restricted to the lower-state energy measurements in the features at 1527 and 1516 nm. These differences could be the result of the highly overlapping nature of these features, leading to erroneous high-temperature line-strength measurements or erroneous line assignments. The overlapping lines of these features, especially at high temperature, introduce the possibility of line-strength uncertainties that are due to the difficulties in the accurate determination of the baseline and the individual peak areas. In addition, the ground-state combination differences line assignment technique employed by Lundsberg-Nielsen *et al*. requires a thorough knowledge of many lines throughout the band, which is a task complicated by the many blended lines. If lines are missing, as was the case for the published research, then the assignment procedure could include some degree of uncertainty. The source of disagreement is currently not clear.

The lower-state energies and reference line strengths can be used to predict the minimum ammonia detectivity for *in situ* combustion monitoring applications. By use of a noise-equivalent absorbance (NEA) of 1.6×10^{-5}, that has been demonstrated for balanced circuit detection schemes[45,46] and a path length $L = 1$ m, the minimum detectivity for the line at 6548.60 cm^{-1} varies from 1.5 parts per million times meter (ppm-m) at room temperature up to 4 ppm-m at 700 K for a signal-to-noise ratio (SNR) of 1 (see Fig. 9).

Table 3 compiles the measured and published spectroscopic parameters for the first feature in Table 2.

Table 3. Comparison of Measured and Published Parameters for the Ammonia Feature at 1531 nm (6528 cm^{-1})

Experimental Data						Published Data								
ν_0	S_0	σ_S	$S_{0,fit}$	E_{fit}''	σ_E	ν_0	S_o	J'	K'	J''	K''	σ	E''	Line
6528.76	0.0624	0.0014	0.0627	277	5	6528.764	0.0373	4	2	5	3	*a*	265.23	*a*
—						6528.827	0.0023							*b*
—						6528.838	0.0022							*c*
6528.89	0.0332	0.0008	0.0333	301	6	6528.894	0.0229							*d*
—						6528.944	0.0010							*e*
6529.11	‡	‡	†	1783	183	—								*f*
6529.18	0.0347	0.0010	0.0348	266	6	6529.184	0.0236	4	2	5	3	*s*	264.52	*g*

The measured parameters include line position, line strength, and lower-state energy along with their respective experimental uncertainties. Table 3 also includes published values for comparison with ν_0 and S_0 from Ref. 39 and E'' from Ref. 32, based on the line assignments and symmetry (J', K', J'', K'', σ) from Ref. 38. Lines *a*, *d*, and *g* in Table 3 show agreement between the published and the measured line positions, but the measured line strengths yield improved values that are 45–70% stronger than the published values. Lines *b*, *c*, and *e* in Table 3 list transitions from the published literature that we did not measure, suggesting that either those transitions do not occur at the specified frequencies or the published line strengths are overpredicted. Line *f* lists a hot line that was not detectable at room temperature but gains in strength with increasing temperature. Tables 4–8 summarize the spectroscopic parameters for the other five features listed in Table 2 in a similar fashion.

Although these tables of measured parameters do not comprise a complete atlas of the ammonia spectrum near 1.5 μm, they do provide improved quantitative values for pertinent spectroscopic parameters for the six ammonia features that have been studied carefully with high resolution. Note that Table 2 suggests sensor applications that are appropriate for each of the six features.

6. Sensor Demonstration

Using the spectroscopic information listed above, we developed and tested a sensor to demonstrate the feasibility of interference-free NH_3 slip monitoring in combustion applications with the absorption feature near 6548 cm^{-1}. The experimental schematic for the sensor is shown in Fig. 10. The combustor consisted of a lean premixed ethylene–air flat-flame atmospheric pressure burner operating at an equivalence ratio of $\phi \approx 0.7$, a vertical exhaust stack, and a 120-cm-long horizontal stack section 79 cm above the burner. Windows at the ends of the 3.8-cm-diameter horizontal section permitted optical ac-

Table 4. Comparison of Measured and Published Parameters for the Ammonia Feature at 1527 nm (6548 cm^{-1})

Experimental Data						Published Data							
ν_0	S_0	σ_S	$S_{0,fit}$	E_{fit}''	σ_E	ν_0	S_o	J'	K'	J''	K''	σ	E''
6548.60	0.0425	0.0010	0.0424	210	6	6548.608	0.0306	3	2	4	3	*s*	165.33
6548.64	0.0015	0.0004	0.0013	880	49	—							
6548.69	‡	‡	0.0003	1055	131	6548.690	0.0009						
—						6548.702	0.0009						
—						6548.723	0.0011						
6548.79	0.0413	0.0011	0.0413	228	6	6548.792	0.0314	3	2	4	3	*a*	166.09
—						6548.860	0.0009						
—						6548.875	0.0009						
—						6548.885	0.0009						
6548.92	0.0088	0.0005	0.0087	228	19	6548.919	0.0076						

Table 5. Comparison of Measured and Published Parameters for the Ammonia Feature at 1522 nm (6568 cm^{-1})

Experimental Data						Published Data							
ν_0	S_0	σ_S	$S_{0,fit}$	E_{fit}''	σ_E	ν_0	S_o	J'	K'	J''	K''	σ	E''
6568.26	0.0039	0.0003	0.0038	570	20	—							
—						6568.298	0.0349						
6568.30	0.0589	0.0014	0.0590	120	12	6568.305	0.0359						
6568.40	0.0577	0.0012	0.0577	122	10	6568.401	0.0394						
6568.46	0.0045	0.0001	0.0045	†	†	6568.463	0.0049						

Table 6. Comparison of Measured and Published Parameters for the Ammonia Feature at 1516 nm (6596 cm^{-1})

Experimental Data						Published Data							
ν_0	S_0	σ_S	$S_{0,fit}$	E_{fit}''	σ_E	ν_0	S_o	J'	K'	J''	K''	σ	E''
6596.20	0.0015	0.0001	0.0015	542	31	6596.206	0.0014						
6596.29	0.0179	0.0005	0.0178	197	19	6596.296	0.0148	3	2	3	1	*a*	116.28
6596.34	0.0125	0.0004	0.0125	83	18	6596.343	0.0117	2	2	2	1	*s*	55.94
6596.38	0.0175	0.0004	0.0175	155	20	6596.382	0.0160	3	2	3	1	*s*	115.54
6596.41	0.0161	0.0007	0.0161	203	29	—							
—						6596.419	0.0163	4	2	4	1	*s*	183.83
6596.43	0.0108	0.0011	0.0108	73	21	—							
6596.53	0.0053	0.0003	0.0053	554	6	6596.534	0.0050						
6596.68	‡	‡	0.0006	1280	6	—							
6596.79	‡	‡	0.0002	888	53	—							

cess for the absorption measurements. The gas temperature along the horizontal section decreased linearly from 530 to 410 K, as measured with a type T thermocouple at 12 locations along the stack.

Gaseous NH_3 was injected into the exhaust 18 cm above the burner to simulate typical Thermal $DeNO_x$ applications, for which NH_3 is injected downstream of the combustion and then allowed to mix with and destroy the NO_x population. In general, methane–air premixed combustion produces the greatest amount of spectral interference because of the large quantities of hot H_2O in the exhaust. However, for the feature at 6548 cm^{-1}, CO_2 interference is prominent. Therefore, for this experiment, ethylene (C_2H_4) was chosen as the fuel to produce greater amounts of CO_2 and to provide a stricter test of the diode-laser sensor.

Table 7. Comparison of Measured and Published Parameters for the Ammonia Feature at 1515 nm (6600 cm^{-1})

Experimental Data						Published Data							
ν_0	S_0	σ_S	$S_{0,fit}$	E_{fit}''	σ_E	ν_0	S_o	J'	K'	J''	K''	σ	E''
6599.81	‡	‡	0.0002	1410	82	—							
6599.89	0.0330	0.0010	0.0330	306	9	6599.893	0.0240						
6599.95	‡	‡	†	987	95	—							
—						6599.961	0.0011						
—						6599.969	0.0009						
—						6599.993	0.0009						
—						6600.004	0.0009						
6600.03	0.0019	0.0004	0.0019	365	35	6660.034	0.0021						
—						6600.053	0.0014						
6600.08	0.0061	0.0008	0.0060	600	10	6660.083	0.0053						
—						6600.116	0.0012						
6600.18	0.0310	0.0009	0.0310	316	6	6660.182	0.0226						
6600.25	‡	‡	†	1381	99	—							

Table 8. Comparison of Measured and Published Parameters for the Ammonia Feature at 1497 nm (6678 cm^{-1})

Experimental Data						Published Data							
ν_0	S_0	σ_S	$S_{0,fit}$	E_{fit}''	σ_E	ν_0	S_o	J'	K'	J''	K''	σ	E''
6678.18	Hot line		†	†	†	—							
6678.27	0.0036	0.0008	0.0038	†	†	—							
—						6678.301	0.0429						
6678.30	0.0637	0.0012	0.0653	157	10	6678.304	0.0429	5	4	4	3	*a*	166.09
—						6678.378	0.0017						
—						6678.394	0.0016						
6678.41	Hot line		†	†	†	6678.407	0.0014						
6678.47	0.0219	0.0012	0.0218	120	6	6678.470	0.0213						
—						6678.524	0.0410						
6678.53	0.0564	0.0021	0.0562	209	8	6678.533	0.0437						
—						6678.611	0.0008						
6678.77	Hot line		†	†	†	—							
6678.79	Hot line		†	†	†	—							

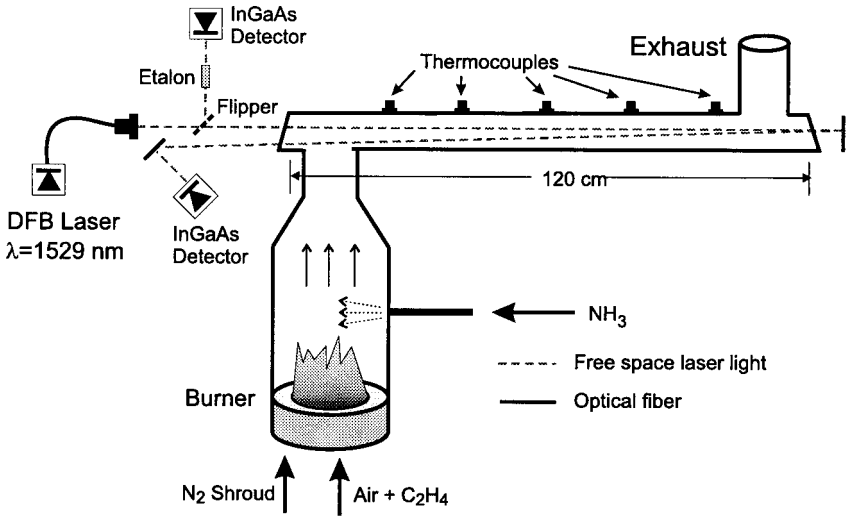

Fig. 10. Schematic for the ammonia slip experiment. Measurements of NH_3 slip in the exhaust of a premixed ethylene–air–ammonia flame are made in a horizontal stack 79 cm above the burner.

The optical system consisted of a fiber-coupled distributed feedback (DFB) diode laser instead of the ECDL, a flipper mirror and solid etalon to measure the laser's frequency variation during tuning, and a two-pass configuration through the exhaust stack for a total path length of 240 cm. The DFB offers the capacity for faster tuning rates, larger tuning depth, and incident intensity that is easier to model with polynomial approximations compared with the ECDL. For the stack measurements, we scanned the DFB at 1250 Hz and used 20 sweep averages to reduce high-frequency noise, yielding a measurement bandwidth of 62.5 Hz (16-ms measurement time) and a NEA of 4×10^{-5}, corresponding to a 5-ppm-m minimum detectivity for a SNR of 1.

Figure 11 shows the measured results for *in situ* monitoring of 22–144 ppm of NH_3 in the exhaust gases into which NH_3 had been seeded. A CO_2 feature at 6548.3 cm^{-1} is shown on the same plot, demonstrating the ammonia feature's avoidance of the spectral interference. Moreover, the areas of the NH_3 features decrease linearly with NH_3 concentration, indicating that there are no hidden H_2O or CO_2 transitions buried underneath the NH_3 feature. Use of frequency modulation[47] or autobalancing circuit techniques[46] should improve the SNR by another order of magnitude, yielding single-digit ppm sensitivities for the *in situ* sensor without interfering absorption from the major combustion products. Therefore the validity of a diode-laser-based NH_3 slip absorption sensor near 1.5 μm, which is capable of measuring ppm concentrations, has been demonstrated.

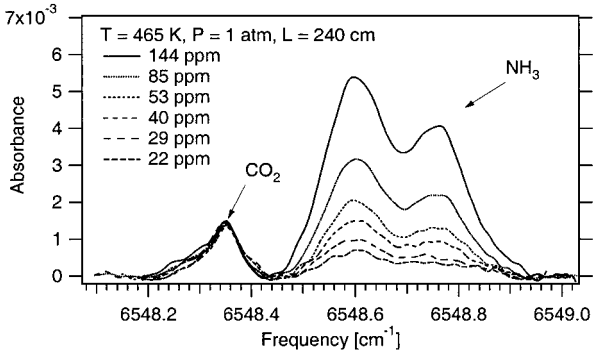

Fig. 11. Measured absorbance data for the NH_3 feature near 6548 cm^{-1} (1527 nm) in the postflame gases above an ethylene–air–ammonia premixed flame (P = 1 atm, L = 240 cm, T = 465 K). A CO_2 feature is shown near 6548.3 cm^{-1}.

7. Conclusions

The spectroscopy of ammonia near 1.5 μm has been thoroughly investigated to select appropriate absorption transitions for *in situ* ammonia monitoring in air-quality and combustion emissions applications by use of diode-laser sensors. Six features were identified that offer a good balance of sensitivity and interference-free detection: three features for air-quality monitoring and three features for emissions monitoring.

We recorded survey spectra in a static cell by tuning a ECDL over its entire range (1496–1582 nm). We made high-resolution absorption measurements of the six selected features by scanning the ECDL approximately 1 cm^{-1} over individual features. Fundamental spectroscopic parameters for the six NH_3 features, including line positions, line strengths, and lower-state energies, were measured in room-temperature and heated static cells. These measured parameters were compared with previously published data, and many discrepancies in the number and strengths of lines were noted. Unlike previously published measurements, the results reported here were obtained in optically thin conditions. Thus we expect that these results are an improvement on the pertinent parameters for the six selected features.

A measurement application was used to demonstrate the capacity for interference-free NH_3 monitoring with diode-laser sensors in the combustion gases above a premixed ethylene–air flame with NH_3 injection. Over a 2.4-m path length, interference-free measurements of 22–144 ppm of NH_3 were demonstrated with a NEA of 4×10^{-5}, verifying the feasibility of the diode-laser sensor near 1.5 μm for *in situ* monitoring of single-digit ppm concentrations of NH_3 slip.

The noise-equivalent detection limit of 5 ppm-m achieved by the research in this paper for isolated ammonia transitions is difficult to compare directly with previously published research for *in situ* monitoring with diode-laser-based sensors. Ahlberg *et al.*[18] claim better than 1-ppm-m sensitivity with a 2-s measurement time for *in situ* combustion exhaust applications, but they do not reveal the wavelengths that were employed, the specific transitions, or the spectroscopic parameters, nor do they verify isolation from carbon dioxide interferences. Modugno and Corsi[21] have selected transitions that can achieve interference-free 4-ppm-m detectivity in room air containing mole fractions of water up to 10%, but do not estimate the detectivity at elevated temperatures pertinent to combustion exhaust and do not verify that the selected ammonia transitions remain isolated from water lines that emerge at elevated temperatures. Monlux *et al.*[20] published *in situ* ammonia measurements in flue gases, but did not specify a detection limit or path length, although a 2-ppm detection limit can be inferred from one of the figures. Moreover, neither the specific ammonia transition nor the wavelengths and spectroscopic parameters for the sensor were specified, nor was isolation from interfering species verified.

The multitude of publications pertaining to ammonia monitoring with diode-laser sensors suggests that the topic is of significant interest to the sensing community, yet the lack of information in most of the papers regarding spectral interferences from flue gas constituents and specific transitions used indicates that more research is needed. Our research makes headway with regard to ammonia monitoring by selecting appropriate transitions, measuring their fundamental spectroscopic parameters, then verifying interference-free measurements in flue gases for one selected feature, and achieving detection limits that are similar to previously published results.

Appendix A: Nomenclature Used in Tables 3–8

ν_0	line center (cm^{-1}),
S_0	line strength (cm^{-2} atm^{-1}) at T_0 = 296 K,
σ_s	standard deviation of the measured line strength S_0 (cm^{-2} atm^{-1}),
$S_{0,\mathrm{fit}}$	line strength (cm^{-2} atm^{-1}) at T_0 = 296 K as determined by an exponential fit to $S(T)$ according to Eq. (3),
E_{fit}''	lower-state energy (cm^{-1}) as determined by an exponential fit to $S(T)$ according to Eq. (3),
σ_E	standard deviation in the fit for measuring E_{fit}'' (cm^{-1}),
J', K'	upper-state symmetric top rotational quantum numbers,
J'', K''	lower-state symmetric top rotational quantum numbers,
σ	transition symmetry: symmetric (*s*) or asymmetric (*a*),
hot line	transition emerges at higher temperatures,
E''	lower-state energy (cm^{-1}) based on transition assignment.

In Tables 3–8, the dash indicates that the transition cannot be seen in the measurements and is not listed in the literature; ‡ indicates that the data were too weak to measure at room temperature; and † indicates that the data could not be determined from the exponential fit.

This research was supported primarily by the Environmental Protection Agency's Office of Research and Development's National Center for Environmental Research Science to Achieve Results research grants program, with additional support from Metrolaser, Inc. through the National Science Foundation Small Business Innovative Research program.

References

1. R. K. Lyon and J. E. Hardy, "Discovery and development of the Thermal DeNO$_x$ process," Ind. Eng. Chem. Fundam. **25,** 19–24 (1986).
2. K. Hjuler and K. Dam-Johansen, "Design of a flue gas probe for ammonia measurement," Anal. Chim. Acta **282,** 703–709 (1993).
3. H. Kassman, L.-E. Åmand, and B. Leckner, "Secondary effects in sampling ammonia during measurements in a circulating fluidised-bed combustor," J. Inst. Energy **70,** 95–101 (1997).
4. V. Nagali, S. I. Chou, D. S. Baer, R. K. Hanson, and J. Segall, "Tunable diode-laser absorption measurements of methane at elevated temperatures," Appl. Opt. **35,** 4026–4032 (1996).
5. R. R. Gamache, Center for Atmospheric Research, University of Massachusetts, Lowell, Lowell, Mass. (personal communication, 1999).
6. A. Goldman, R. R. Gamache, A. Perrin, J.-M. Flaud, C. P. Rinsland, and L. S. Rothman, "HITRAN partition functions and weighted transition-moments squared," J. Quant. Spectrosc. Radiat. Transfer **66,** 455–486 (2000).
7. R. S. McDowell, "Rotational partition functions for symmetric-top molecules," J. Chem. Phys. **93,** 2801–2811 (1990).
8. R. J. Willey and M. F. Fox, "Ammonia decomposition over 430-SS etched metal catalysts," J. Catal. **112,** 590–594 (1988).
9. N. Jacquinet-Husson, E. Arie, J. Ballard, A. Barbe, G. Bjoraker, B. Bonnet, L. R. Brown, C. Camy-Peyret, J. P. Champion, A. Chedin, A. Chrusin, C. Clerbaux, G. Duxbury, J.-M. Flaud, N. Fourrie, A. Fayt, G. Graner, R. Gamache, A. Goldman, V. Golovko, G. Guelachvili, J.-M. Hartmann, J. C. Hilico, J. Hillman, G. Lefevre, E. Lellouch, S. N. Mikhailenko, O. V. Naumenko, V. Nemtchinov, D. Newnham, A. Nikitin, J. Orphal, A. Perrin, D. C. Reuter, C. P. Rinsland, L. Rosenmann, L. S. Rothman, N. A. Scott, J. Selby, L. N. Sinitsa, J. M. Sirota, A. M. Smith, K. M. Smith, V. G. Tyuterev, R. H. Tipping, S. Urban, P. Varanasi, and M. Weber, "The 1997 spectroscopic GEISA databank," J. Quant. Spectrosc. Radiat. Transfer **62,** 205–254 (1999).
10. L. S. Rothmann, C. P. Rinsland, A. Goldman, S. T. Massie, D. P. Edwards, J.-Y. Mandin, J. Schroeder, A. McCann, R. R.

Gamache, R. B. Wattsin, K. Yoshino, K. V. Chance, K. W. Juck, L. R. Brown, V. Nemtchechin, and P. Varanasi, "The HITRAN molecular spectroscopic database and HAWKS (HITRAN atmospheric workstation): 1996 edition," J. Quant. Spectrosc. Radiat. Transfer **60,** 665–710 (1998).
11. M. Ohtsu, H. Kotani, and H. Tagawa, "Spectral measurements of NH_3 and H_2O for pollutant gas monitoring by 1.5-μm InGaAsP/InP lasers," Jpn. J. Appl. Phy. **22,** 1553–1557 (1983).
12. T. Yanagawa, S. Saito, and Y. Yamamoto, "Frequency stabilization of 1.5-μm InGaAsP distributed feedback laser to NH_3 absorption lines," Appl. Phys. Lett. **45,** 826–828 (1984).
13. M. Fehér, P. A. Martin, A. Rohrbacher, A. M. Soliva, and J. P. Maier, "Inexpensive near-infrared diode-laser-based detection system for ammonia," Appl. Opt. **32,** 2028–2030 (1993).
14. L. I. Gurinovich, V. P. Duraev, V. A. Ivanov, and N. K. Nikeenko, "Application of near IR band injection lasers for the control of ammonia content in air," J. Appl. Spectros. **58**(3–4), 240–245 (1993).
15. T. Wu, H. An, P. Jiang, Y. Fang, S. Tao, and P. Ye, "Spectral measurements of NH_3 absorption lines by a 1.5-μm grating-external-cavity semiconductor laser," Opt. Lett. **18,** 729–731 (1993).
16. M. Fehér, Y. Jiang, J. P. Maier, and A. Miklós, "Optoacoustic trace-gas monitoring with near-infrared diode lasers," Appl. Opt. **33,** 1655–1658 (1994).
17. H. Ahlberg, S. Lundqvist, R. Tell, and T. Andersson, "Industrialized high sensitivity fiber-optic near-IR diode laser based gas analysis system," in *Tunable Diode Laser Spectroscopy, Lidar, and DIAL Techniques for Environmental and Industrial Measurements*, H. I. Schiff, A. Fried, and D. K. Killinger, eds., Proc. SPIE **2112,** 118–129 (1994).
18. H. Ahlberg, S. Lundqvist, R. Tell, and T. Andersson, "Laser spectroscopy for in situ ammonia monitoring," Spectros. Eur. **6**(2), 22–26 (1994).
19. J. P. Dakin, H. O. Edwards, and B. H. Weigl, "Latest developments in gas sensing using correlation spectroscopy," in *Chemical, Biochemical, and Environmental Fiber Sensors VII*, A. V. Scheggi, ed., Proc. SPIE **2508,** 2–17 (1995).
20. G. Monlux, J. A. Brand, P. Zmarzly, M. Walker, K. W. Groff, G. J. Fetzer, N. Goldstein, F. Bein, S. C. Richtsmeier, and J. Lee, "In situ ammonia analyzer for process control and environmental monitoring," in *Advanced Technologies for Environmental Monitoring and Remediation*, T. V.-Dinh, ed., Proc. SPIE **2835,** 236–247 (1996).
21. G. Modugno and C. Corsi, "Water vapour and carbon dioxide interference in the high sensitivity detection of NH_3 with semiconductor diode lasers at 1.5 μm," Infrared Phy. Technol. **40,** 93–99 (1999).
22. S. Urban, "High-resolution infrared spectroscopy of ammonia: a survey of theory and analyses of spectra," J. Quant. Spectrosc. Radiat. Transfer **48,** 675–684 (1992).
23. W. S. Benedict and E. K. Plyler, "Vibration-rotation bands of ammonia: II. The molecular dimensions and harmonic frequencies of ammonia and deuterated ammonia," Can. J. Phys. **35,** 1235–1241 (1957).
24. H. J. Unger, "Infrared absorption bands of ammonia," Phys. Rev. **43,** 123–128 (1933).
25. W. S. Benedict, E. K. Plyler, and E. D. Tidwell, "Vibration-rotation bands of ammonia: 1. The combination bands $\nu_2 + (\nu_1, \nu_3)$," J. Res. Natl. Bur. Stand. **61**(3), 123–147 (1958).
26. W. S. Benedict, E. K. Plyler, and E. D. Tidwell, "Vibration-rotation bands of ammonia: III. The region 3.2-4.3 microns," J. Chem. Phys. **29,** 829–845 (1958).
27. J. S. Garing, H. H. Nielsen, and K. Narahari Rao, "The low-frequency vibration rotation bands of the ammonia molecule," J. Mol. Spectros. **3,** 496–527 (1959).
28. P. Varanasi, "Shapes and widths of ammonia lines collision-broadened by hydrogen," J. Quant. Spectrosc. Radiat. Transfer **12,** 1283–1289 (1972).
29. J. S. Margolis and S. Sarangi, "Measurement of hydrogen- and self-broadened half-widths of ammonia at 200 and 300 °K," J. Quant. Spectrosc. Radiat. Transfer **16,** 405–408 (1976).
30. S. Sarangi, "Analysis of the $\nu_3 + \nu_4$ band of ammonia," J. Quant. Spectrosc. Radiat. Transfer **18,** 257–288 (1977).
31. S. Sarangi, "Analysis of line intensities in the two-micron band of ammonia," J. Quant. Spectrosc. Radiat. Transfer **18,** 289–293 (1977).
32. Š. Urban, R. D'Cunha, K. Narahari Rao, and D. Papoušek, "The $\Delta k = \pm 2$ 'forbidden band' and inversion-rotation energy levels of ammonia," Can. J. Phys. **62,** 1775–1791 (1984).
33. E. Lellouch, N. Lacome, G. Guelachvili, G. Tarrago, and T. Encrenaz, "Ammonia: experimental absolute linestrengths and self-broadening parameters in the 1800- to 2100-cm^{-1} range," J. Mol. Spectros. **124,** 333–347 (1987).
34. G. Guelachvili, A. H. Abdullah, N. Tu, K. Narahari Rao, Š. Urban, and D. Papoušek, "Analysis of high-resolution Fourier transform spectra of $^{14}NH_3$ at 3.0 μm," J. Mol. Spectros. **133,** 345–364 (1989).
35. Š. Urban, N. Tu, K. Narahari Rao, and G. Guelachvili, "Analysis of high-resolution Fourier transform spectra of $^{14}NH_3$ at 2.3 μm," J. Mol. Spectros. **133,** 312–330 (1989).
36. B. B. Radak, J. I. Lunine, D. M. Hunten, and G. H. Atkinson, "Line intensities in the 647.5-nm ammonia band at low temperatures determined by intracavity laser spectroscopy," J. Quant. Spectrosc. Radiat. Transfer **53,** 519–526 (1995).
37. L. R. Brown and J. S. Margolis, "Empirical line parameters of NH_3 from 4791 to 5294 cm^{-1}," J. Quant. Spectrosc. Radiat. Transfer **56**(2), 283–294 (1996).
38. L. Lundsberg-Nielsen, F. Hegelund, and F. M. Nicolaisen, "Analysis of the high-resolution spectrum of ammonia ($^{14}NH_3$) in the near-infrared region, 6400-6900 cm^{-1}," J. Mol. Spectros. **162,** 230–245 (1993).
39. L. Lundsberg-Nielsen, "Molecular overtone spectroscopy on ammonia," Ph.D. dissertation (Department of Chemistry, University of Copenhagen, Copenhagen, Denmark, and the Danish Institute of Fundamental Metrology, Lygnby, Denmark, 1995).
40. L. Sandström, H. Ahlberg, S. Höjer, A. G. Larsson, and S. Bäckström, "Near-infrared semiconductor lasers for gas analysis operating in the 2-μm range," in *Conference on Lasers and Electro-Optics*, Vol. 9 of OSA 1996 Technical Digest Series (Optical Society of America, Washington, D.C., 1996), pp. 239–240.
41. E. R. Furlong, R. M. Mihalcea, M. E. Webber, D. S. Baer, and R. K. Hanson, "Diode-laser sensors for real-time control of pulsed combustion systems," AIAA J. **37,** 732–737 (1999).
42. G. Herzberg, *Molecular Spectra and Molecular Structure II: Infrared and Raman Spectra of Polyatomic Molecules* (Krieger, Malabax, Fla., 1991).
43. Š. Urban, D. Papoušek, V. Malathy Devi, B. Fridovich, R. D'Cunha, and K. Narahari Rao, "Transition dipole matrix elements for $^{14}NH_3$ from the line intensities of the $2\nu_2$ and ν_4 bands," J. Mol. Spectros. **106,** 38–55 (1984).
44. A. S. Pine, V. N. Markov, G. Buffa, and O. Tarrini, "N_2, O_2, H_2, Ar and He broadening in the ν_1 band of NH_3," J. Quant. Spectrosc. Radiat. Transfer **50**(4), 337–348 (1993).
45. R. M. Mihalcea, "CO and CO_2 measurements in combustion environments using external cavity diode lasers," Ph.D. dissertation (High Temperature Gasdynamics Laboratory, Department of Mechanical Engineering, Stanford University, Stanford, Calif., 1999).
46. P. C. D. Hobbs, "Ultrasensitive laser measurements without tears," Appl. Opt. **36,** 903–920 (1997).
47. J. A. Silver, "Frequency-modulation spectroscopy for trace species detection: theory and comparison among experimental methods," Appl. Opt. **31,** 707–717 (1992).